

Phase diagrams of Bose-Hubbard model and Haldane-Bose-Hubbard model with complex hopping amplitudes

Yoshihito Kuno, Takashi Nakafuji, and Ikuo Ichinose

¹*Department of Applied Physics, Nagoya Institute of Technology, Nagoya 466-8555, Japan*

(Dated: July 23, 2018)

In this paper, we study Bose-Hubbard models on the square and honeycomb lattices with complex hopping amplitudes, which are feasible by recent experiments of cold atomic gases in optical lattices. To clarify phase diagrams, we use an extended quantum Monte-Carlo simulations (eQMC). For the system on the square lattice, the complex hopping is realized by an artificial magnetic field. We found that vortex-solid states form for certain set of magnetic field, i.e., the magnetic field with the flux quanta per plaquette $f = p/q$, where p and q are co-prime natural numbers. For the system on the honeycomb lattice, we add the next-nearest neighbor complex hopping. The model is a bosonic analog of the Haldane-Hubbard model. By means of the eQMC, we study the model with both weak and strong on-site repulsions. Numerical study shows that the model has a rich phase diagram. We also found that in the system defined on the honeycomb lattice of the cylinder geometry, an interesting edge state appears.

PACS numbers: 03.75.Hh, 67.85.Hj, 64.60.De

I. INTRODUCTION

Cold atoms in an optical lattice (OL) have been used as versatile quantum simulators for the last decade. In particular, the Bose gas system is highly controllable and has a rich phase diagram as a strongly-correlation system[1]. Recently, generation of an artificial magnetic field in cold atom systems was experimentally succeeded by using laser-assisted tunneling in a tilted optical potential[2, 3], whose theoretical proposal was given by Jaksch and Zoller[4]. These experimental methods can create a stronger magnetic field compared to that generated by rotating optical lattice[5], and therefore it is expected that a strong-magnetic field regime corresponding to, e.g., the quantum Hall state is realized in cold atom systems.

Bose gas system in a strong magnetic field has been studied very actively in the last several years. In particular, study on two-component Bose gas system in a strong magnetic field in the continuum space predicts a bosonic analog of integer quantum Hall state (IQHS) for certain inter and intra-repulsions[6]. Generation of an incompressible vortex liquid was also suggested in a similar parameter region of Bose system in a strong magnetic field[7]. On the other hand for the Bose gas system on the optical lattice, the numerical exact diagonalization suggests an existence of a bosonic Laughlin state[8, 9], and also a new kind of fractional quantum Hall state[10].

There are many studies on the lattice boson systems with a dilute particle density and in a weak magnetic field[11, 12]. Formation of the vortex solid was predicted there. However for the system of interacting bosons in a strong magnetic field, the structure of the ground-state, in particular, structure of all the vortex-solid states are not known. Study on the complete global phase diagram of the system for various hopping amplitude, interactions, magnetic-field strength and particle filling, etc., is still missing. For lattice boson systems and certain related

models in strong magnetic regime, a number of works have been reported so far. For classical spin models, Choi and Doniach[13] found by an analytical method that the uniformly frustrated two-dimensional (2D) XY model has stable vortex-solid ground-states at $f = 1/2, 1/3$ and $1/4$, where f is the magnetic flux quanta per the fundamental plaquette. Also, some of vortex-solid states were predicted by using Monte-Carlo simulations[14–16] and a Gross-Pitaevskii theory[17, 18]; these studies showed some vortex-solid patterns for the 2D classical model at $f = 1/2, 1/3$ and $1/4$. Our previous study by using effective theory and Monte-Carlo simulations also predicted some solid patterns at $f = 1/2, 1/3$ in two component lattice boson system assuming commensurate particle density[19].

In theoretical models describing systems in a magnetic field, the hopping amplitudes acquire a nontrivial phase and become complex numbers. As a result, there appear various interesting phases, some of which are aforementioned vortex solid, the bosonic Laughlin state, etc. In the first half of the present paper, we clarify various vortex ground-states of a Bose Hubbard model (BHM) in a strong magnetic field by using extended quantum Monte-Carlo simulations (eQMC), in which effects of both phase and density fluctuations of the boson field are taken into account properly in the path-integral formalism. We found that a phase transition from the vortex solid to vortex liquid takes place as the on-site repulsion U is varied. In the second half of the paper, we study a bosonic analog of the Haldane model on the honeycomb lattice with the on-site repulsion U , which is sometimes called Haldane-Bose-Hubbard model (HBHM). Besides the nearest-neighbor (NN) hopping, the HBHM contains the next-NN (NNN) hopping with a nontrivial phase ϕ . The Haldane model was originally proposed as a fermion model that has the ground-state similar to the quantum Hall state[20]. In the recent paper[21], the HBHM with $\phi = \pi/2$ was studied by the dynamical mean-field theory

and an exact diagonalization of a small system. In this paper, we study the HBHM by the eQMC for both strong and weak on-site repulsion. We exhibit the global phase diagram, which should be compared with that obtained in Ref.[21], detailed critical behaviors of the phase transitions, physical properties of an edge state in a cylinder geometry, etc.

This paper is organized as follows. In Sec.II, we introduce the BHM in an artificial magnetic field and explain the derivation of the effective theory, which will be studied by the eQMC. In Sec.III, we explain some details of the eQMC show the global phase diagram, which is obtained by the eQMC. In the phase diagram, there exist various vortex-solid states and also vortex quantum liquid states for certain specific magnitude of the magnetic field. Phase transition from the disordered state to vortex solid is studied by the finite size scaling and the critical exponents are estimated. In Sec.IV, the BHM in an magnetic field is studied by using a duality transformation and origin of the vortex-solid patterns found in Sec.III is explained. Phase diagram obtained by varying boson density is also shown. From these observation, possibility of bosonic Laughlin state is discussed by using a Chern-Simons theory. In Sec.V, the phase diagram of the HBHM is obtained, which has four phases. Detailed study of each phase is given by calculating the expectation value of the current and phase correlation on links. Finally we investigate the HBHM in a cylinder geometry, in particular, we are interested in the edge state. Sec.VI is devoted for conclusion.

II. BOSE HUBBARD MODEL IN A UNIFORM MAGNETIC FIELD AND THE EFFECTIVE MODEL

In this section, we consider the BHM defined on a two dimensional (2D) square lattice. We start with the BH Hamiltonian in an artificial magnetic field with a vector potential $A_\mu(r)$,

$$H_{\text{BH}} = -J \sum_{r,\mu} a_r^\dagger e^{-iA_\mu(r)} a_{r+\mu} + \text{h.c.} + \sum_r U n_r^2, \quad (1)$$

where r denotes sites of the lattice and $\mu = \hat{x}, \hat{y}$ is the direction index and it sometimes denotes the unit vector. $a_r (a_r^\dagger)$ is a bosonic annihilation (creation) operator and $n_r = a_r^\dagger a_r$. J is hopping amplitude and U is on-site repulsive interaction. All these parameters are highly controllable in experiments[1]. $A_\mu(r)$ represents a uniform magnetic field perpendicular to the lattice plane. In the numerical calculation, we use

$$A_\mu(r) = \begin{cases} -2\pi f y & (\mu = \hat{x}) \\ 0 & (\mu = \hat{y}) \end{cases}, \quad (2)$$

where $r = (x, y)$ and f is the magnitude of the magnetic flux per plaquette, and its range is $0 \leq f \leq 1$ due to

compactness of the phase degrees of freedom. The gauge field $A_\mu(r)$ creates the uniform magnetic field B_z ; $B_z = \sum_p A_p = 2\pi f$, where p denotes a directed close path around a plaquette and A_p is the vector potential on the path. This model is experimentally feasible[3].

In the following sections, we shall study the BHM in Eq.(1) by the numerical MC simulations. To this end, we have to derive an effective model for the BHM with a *positive definite action*. Although it is difficult to perform the direct quantum simulations because of the complex hopping in Eq.(1), we can derive a useful effective model including relevant quantum effects by integrating out certain degrees of freedom in the path-integral formalism.

In previous work[19], we derived the effective model for some related bosonic systems, and the effective model obtained there was numerically studied by the MC simulations. In this paper, we shall extend the previous methods in order to search inhomogeneous states as a ground state.

Let us start the derivation of the effective model mentioned above. We first parameterize the boson variables in the path integral as $a_r = \sqrt{\rho_r + \delta\rho_r} e^{i\theta(r)}$, where ρ_r is the mean density at site r , which is regarded as *variational parameter* in the MC simulation (see later discussion). On the other hand, the variable $\delta\rho_r$ represents *quantum fluctuation* of the density around the mean value ρ_r , and then the Berry phase term in the action is given as $(\partial_\tau \theta(r))\delta\rho_r$, where the variable $\theta(r)$ is the phase of the boson field. By substituting the above parameterization, the partition function of the BHM defined by Eq.(1) is given as follows by using the imaginary-time τ ,

$$Z_{\text{BH}} = \int [d\delta\rho_r][d\theta(r)] e^{-S_{\text{BH}}}, \quad (3)$$

$$S_{\text{BH}} = \int d\tau \left(\sum_r i(\partial_\tau \theta(r))\delta\rho_r - \sum_{r,\mu} J \sqrt{\rho_r \rho_{r+\mu}} \cos(\theta(r) - \theta(r+\mu) + A_\mu(r)) + J\mathcal{T}(\rho, \theta)\delta\rho + \sum_r (U\rho_r^2 + U\delta\rho_r^2 + 2U\rho_r\delta\rho_r) \right), \quad (4)$$

where $J\mathcal{T}(\rho, \theta)\delta\rho$ denotes the first-order contribution of the quantum fluctuation $\{\delta\rho_r\}$ in the hopping term J , and we have neglected the higher-order terms of $\{\delta\rho_r\}$ coming from the J -terms. As explain in the following section, we determine $\{\rho_r\}$ by the minimum-energy condition in the MC calculation. Therefore the terms of $O(\delta\rho)$ in Eq.(4), except the Berry phase, cancel with each other. Then in Eq.(3), we perform the Gaussian integral for the density fluctuation $\delta\rho_r$ to derive the effective theory whose action is denoted by S_{qXY} . Henceforth, we call this effective model S_{qXY} the *quantum XY model*

(qXYM), whose partition function is given by

$$Z_{\text{qXY}} = \int [d\theta(r)] e^{-S_{\text{qXY}}}, \quad (5)$$

$$S_{\text{qXY}} = \int d\tau \left(\sum_r \frac{1}{4U} (\partial_\tau \theta(r))^2 - J \sum_{r,\mu} \sqrt{\rho_r \rho_{r+\mu}} \cos(\theta(r) - \theta(r+\mu) + A_\mu(r)) + \sum_r U \rho_r^2 \right). \quad (6)$$

Here it should be remarked that S_{qXY} in Eq.(6) is real, and then the standard MC simulation is applicable for the numerical study of the system. Moreover it should be noticed that this model has the *Lorentz symmetry* and therefore it is expected that an excitation corresponding to the *Higgs mode* exists[19, 22]. In fact this mode has been observed in optical lattice experiments[23].

III. EXTENDED QUANTUM MONTE-CARLO SIMULATION

In this section, we numerically study the qXYM by means of the eQMC explained in the previous section. In particular, we are interested in vortex dynamics induced by the strong artificial magnetic field with the vector potential $A_\mu(r)$, and obtain a global phase diagram of vortex states. For the study on phase diagram of the present system with the complex hopping amplitudes, the qXYM is quite useful as the phase degrees of freedom of the boson field plays an essentially important role.

For the eQMC, we put the lattice spacing of the OL, a_L , to the unit of length and also introduce a discretized lattice for the imaginary-time τ with the lattice spacing $\Delta\tau$. Thus, the qXYM becomes a kind of 3D XY model defined on the space-time lattice, whereas its coefficients depend on the variational parameters $\{\rho_r\}$. The lattice action of the qXYM is given as follows:

$$\begin{aligned} S_{\text{qXY}}^L &= \sum_r -\frac{1}{4U\Delta\tau} \cos(\theta(r) - \theta(r - \hat{\tau})) \\ &\quad - J\Delta\tau \sum_{r,\mu} \sqrt{\rho_r \rho_{r+\mu}} \cos(\theta(r) - \theta(r+\mu) + A_\mu(r)) \\ &\quad + \sum_r U\Delta\tau \rho_r^2, \\ &\equiv \sum_r -\frac{1}{4U\Delta\tau} \cos(\theta(r) - \theta(r - \hat{\tau})) + H_{\text{qXY}}, \end{aligned} \quad (7)$$

where r denotes sites on the 3D lattice.

Here we briefly explain the eQMC to study the qXYM of Eq.(7). The qXYM action on path integral includes both the variational parameters $\{\rho_r\}$ and the dynamical phase variables $\theta(r)$'s. We determine the variational variables $\{\rho_r\}$ by the minimum-energy condition by using

MC methods. More precisely, we express the extended partition function $[Z_{\text{qXY}}^L]$ of Eq. (7) as

$$\begin{aligned} [Z_{\text{qXY}}^L] &\equiv \int [d\rho_r] Z_{\text{qXY}}^L(\{\rho_r\}), \\ Z_{\text{qXY}}^L(\{\rho_r\}) &= \int [d\theta(r)] e^{-S_{\text{qXY}}^L}. \end{aligned} \quad (8)$$

In the practical calculation of Eq.(8), we treat $\{\rho_r\}$ as slow variables in the MC local-update with keeping the mean value of $\{\rho_r\}$ constant. On the other hand, we perform the MC simulation for the dynamical variables $\theta(r)$ as the ordinary variables for the fixed $\{\rho_r\}$. From the experience, e.g. in Ref.[24], we know that $\{\rho_r\}$ are quite stable under local updates for given values of parameters in the qXYM action. In the present study, we verified this stable behavior of $\{\rho_r\}$ for typical configurations of $\theta(r)$, i.e., once $\{\rho_r\}$ is selected for fixed parameters of S_{qXY}^L by the MC method, $\{\rho_r\}$ does not change strongly for various configurations of $\theta(r)$.

In the practical calculation, we employ the standard Metropolis algorithm with the local update[25]. The typical sweep measurement is $(50000 - 150000) \times (5 \text{ samples})$, and the acceptance ratio is 40-50%. Errors are estimated from 20 samples by the jackknife method. Here we employ the *canonical ensemble*, and therefore the mean total number of boson, $\sum_r \rho_r$, is conserved during MC updates. This situation is suitable for real experiments of the OL[1]. We employ the periodic boundary condition and the lattice size is L^3 , where L is the linear system size.

$\Delta\tau$ has a relation, $\Delta\tau L = 1/(k_B T)$, thus its dimension is $1/(\text{energy})$. In our calculation, we set $\Delta\tau = 1$, regarded as unit of inverse of energy depending on system temperature. To identify the phase boundary, we calculate the internal energy E and “specific heat” C that are defined as follows,

$$E = \langle H_{\text{qXY}} \rangle / L^3, \quad C = \langle (H_{\text{qXY}} - EL^3)^2 \rangle / L^3, \quad (9)$$

where $\langle \dots \rangle$ means the expectation value calculated as in Eq.(8),

$$\begin{aligned} \langle \dots \rangle &\equiv \int [d\rho_r] \langle \dots \rangle (\{\rho_r\}), \\ \langle \dots \rangle (\{\rho_r\}) &= \int [d\theta(r)] (\dots) e^{-S_{\text{qXY}}^L}. \end{aligned} \quad (10)$$

In Fig.1, we show the global phase diagram obtained by the eQMC for $J = 5.0$, and $\bar{\rho} = 2.0$ ($\bar{\rho}$ is the mean density per site, i.e., $\bar{\rho} = \langle \rho_r \rangle$). The phase diagram is shown in the $(f - U)$ plane and especially we focus on the magnetic flux regime $1/9 \leq f \leq 1/2$.

By calculating the Bose correlation function $\langle a_r^\dagger a_{r'} \rangle$ by means of the eQMC, we have verified that for $f = 0$ and a sufficiently large hopping J , a SF with the long-range order of the phase $\theta(r)$ forms, i.e., $\langle a_r^\dagger a_{r'} \rangle \rightarrow c \neq 0$ for $|r - r'| \rightarrow \infty$. As the value of f is increased, however, the SF order disappears at $f \simeq 0.02$. This implies that the

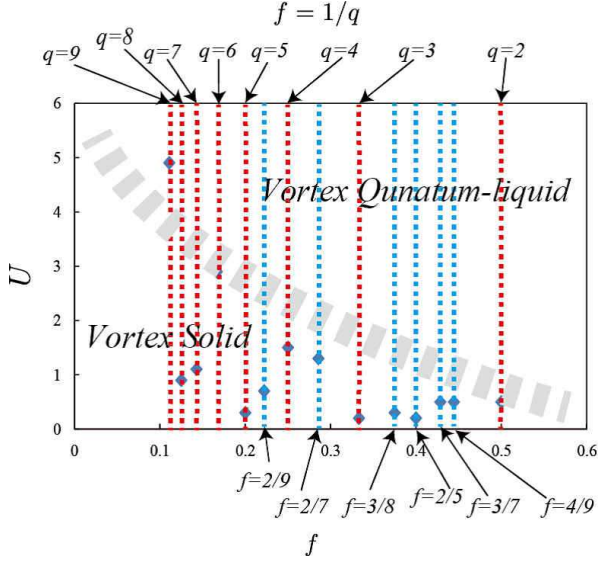


FIG. 1. (Color online) Phase diagram in f - U plane. The red-dotted lines indicates the $f = 1/q$ vortex solid states and the blue-dotted lines the $f = p/q$ vortex solid states. The phase boundary between the solid states and the vortex quantum-liquid states is determined by the behavior of vortex lines in the imaginary time direction. See Fig.5. $J = 5$.

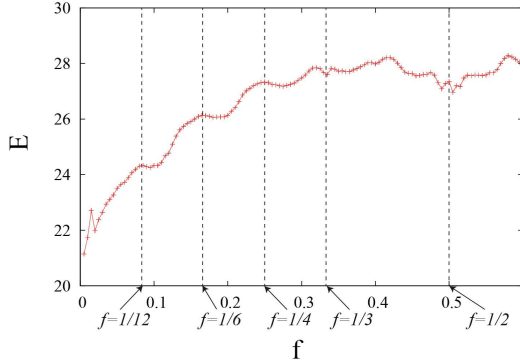


FIG. 2. (Color online) The internal energy E as a function of the strength of the magnetic flux f . At $f \simeq 0.02$, there exists a sharp peak that indicates a phase transition. Correlation function indicates that the system loses the SF at that point. $J = 5$ and $U = 10$. Calculated E indicates the existence of stable states (local minimums) for certain values of f like $f = \frac{1}{2}$ and $\frac{1}{3}$, whereas at $f = \frac{1}{4}$, $\frac{1}{6}$ and $\frac{1}{12}$, a plateau appears. System size $L = 12$.

critical magnetic field $B_c \sim 2\pi \times 0.02$. The internal energy E shown in Fig.2 exhibits a sharp peak at $f \simeq 0.02$, and therefore the phase transition seems to be of first order. As the value of f is increased furthermore, we found that at specific values of f like $f = p/q$, where p and q are co-prime integers, stable vortex-solid states form. We searched such a state for $1/9 \leq f \leq 1/2$ and identified fourteen states. In the free electron lattice system in a uniform magnetic field, specific states for general $f = p/q$

were predicted by Hofstadter[26].

In Fig.1, the observed vortex solid states are indicated in the red- and blue-dotted lines for $J = 5$ and their snapshots are shown in Fig.3. We define vorticity $\Omega(r')$ on the dual site r' of the site r as follows:

$$\begin{aligned} \Omega(r') = \frac{1}{4} & \left[\sin(\theta(r + \hat{x}) - \theta(r) + A_{\hat{x}}(r)) \right. \\ & + \sin(\theta(r + \hat{x} + \hat{y}) - \theta(r + \hat{x}) + A_{\hat{y}}(r + \hat{x})) \\ & + \sin(\theta(r + \hat{y}) - \theta(r + \hat{x} + \hat{y}) - A_{\hat{x}}(r + \hat{y})) \\ & \left. + \sin(\theta(r) - \theta(r + \hat{y}) - A_{\hat{y}}(r)) \right]. \end{aligned} \quad (11)$$

Expectation value of $\Omega(r')$ is calculated by the eQMC rather straightforwardly.

We have found that the formation of vortex solid state depends on the lattice size L ; i.e., for the $f = p/q$ vortex solid state to form, the spacial lattice size must be $qN \times qM$ (N and M are natural numbers). As seen in Fig.3, the quantized vortices are pinned at sites of the dual lattice of the OL and they form solid pattern. In our previous study[19] by the Monte-Carlo simulation assuming a homogeneous density of boson, some specific vortex solids (e.g., $f = 1/2, 1/3$ and $1/4$) were found. However in the present study using the eQMC, we found more general solid patterns $f = p/q$. This is due to the fact that the spatial density modulations are included as the variational parameter $\{\rho_r\}$ in the eQMC. As the density fluctuations suppress the fluctuations of the phase degrees of freedom through the quantum uncertainty relation, and then the stable vortex solid formation is enhanced in the present study. Behavior of the “specific heat” C as a function of the hopping J for $f = \frac{1}{2}$ and $\frac{1}{3}$ is shown in Fig.4. The results indicate the second-order phase transitions from the vortex solid to the disordered state as J is decreased.

In Fig.3, we also show snapshots for incommensurate (‘irrational’) magnetic flux $f \sim 0.23$ and 0.27 . It is obvious that vortices are located in sites of the dual lattice but they do not form a regular crystalline pattern. However they are rather stable against the MC updates. Therefore we conclude that an *amorphous state* of vortex forms at such fillings, although at the fillings belonging to the plateaus in Fig.2, a regular vortex lattice is to be maintained by the lattice pinning effect.

As we explained above, the density fluctuation influences the dynamics of the phase degrees of freedom $\theta(r)$. Therefore it is interesting to see how the vortex behavior changes with the strength of the on-site repulsion U . Numerical simulation for the $f = p/q$ vortex solid state shows that as the value of U increases, the vortex-lines in the imaginary-time direction starts to fluctuate. In Fig.5, we show the typical vortex-lines in the $f = 1/3$ and $1/4$ cases. When U is small, $U = 0.1$, the vortex-lines are straight in the imaginary time direction, whereas for large U , $U = 10$, the vortex-lines are entangled with each other, i.e., the regular vortex lattices shown in Fig.3 at some spatial layer tend to distort in adjacent layers and

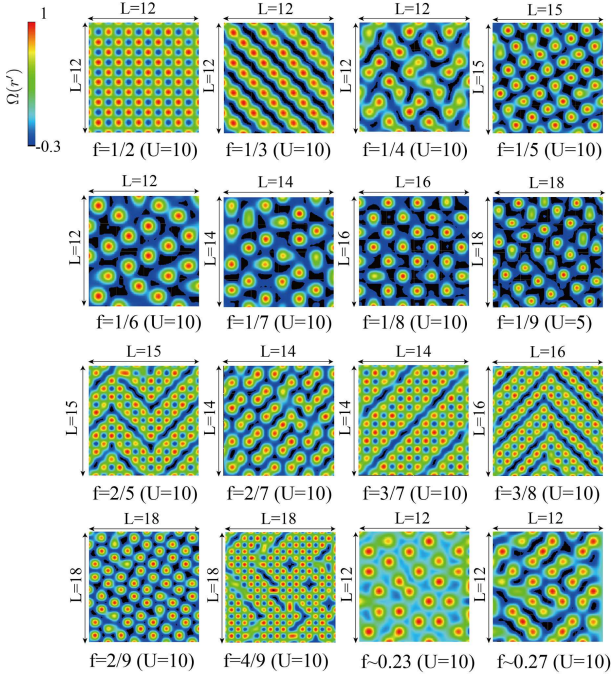


FIG. 3. (Color online) Snapshots of vortex $\Omega(r')$ for $\bar{\rho} = 2.0$ and $J = 5$. They show vortex solid states in $f = p/q$ ($1/9 \leq f \leq 1/2$). The results indicate 14 patterns of the vortex solid states, which are all of possible combinations of coprime numbers p and q . For $f = \frac{1}{2}$ and $\frac{1}{3}$, the rigid patterns appear, whereas for $f = \frac{1}{4}$ and $\frac{1}{6}$ locations of vortices are slightly loose. On the other hand for incommensurate f 's (0.23 and 0.27), vortices do not form a lattice.

then the parallel-translated regular lattices reappear in some other layers. This different behavior of the vortex line stems from the quantum fluctuation, i.e., whether the degenerate vortex solid states in 2D are superposed or not through *quantum tunneling* processes. When the degenerate states in 2D are superposed, the state may be regarded as a *vortex quantum-liquid* state. As shown in the phase diagram in Fig.1, the phase boundary between the vortex solid phase and the vortex quantum-liquid phase exists. However the phase boundary is not clear because the U -dependent term in S_{qXY}^L in Eq.(7) generates only one-dimensional effect. Here we conclude that *the on-site interaction U melts the rigid vortex-line states into the fluctuating vortex line states*. In following section, the observed phenomenon in the above is studied by using a duality transformation of the qXYM.

Finally, by using the finite-size scaling (FSS) of C , we numerically obtain the values of the critical exponents. See Fig.4. By the FSS hypothesis, C for the system size L , $C_L(\epsilon)$, is parametrized as

$$C_L(\epsilon) = L^{\sigma/\nu} \Phi(L^{1/\nu} \epsilon^\nu), \quad (12)$$

where $\Phi(x)$ is a scaling function and $\epsilon = (J - J_\infty)/J_\infty$ with the critical coupling J_∞ for the system $L \rightarrow \infty$. In Eq.(12), σ and ν are critical exponent, in particular, ν is the critical exponent of the correlation length $\xi \propto$

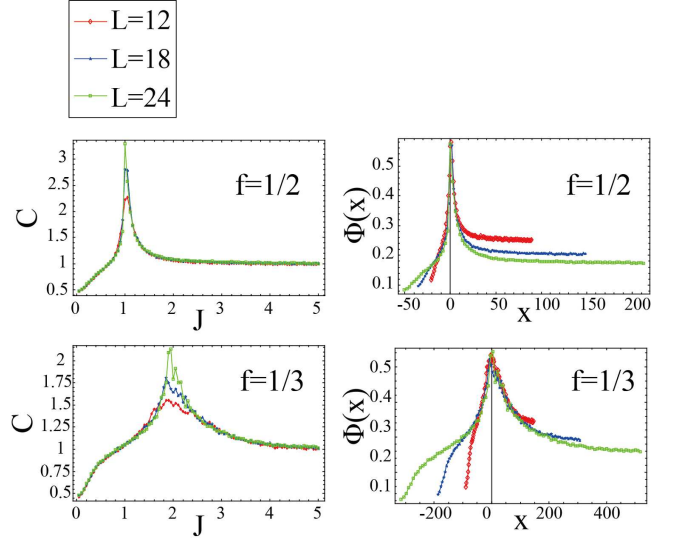


FIG. 4. (Color online) Specific heat C for the system size $L = 12, 18$ and 24 . Scaling function of the FSS for $f = \frac{1}{2}$ and $f = \frac{1}{3}$.

$|J - J_\infty|^{-\nu}$. The results of the FSS are shown in Fig.4 for $f = 1/2$ and $1/3$. The critical exponents are estimated as $\nu = 0.80(0.55)$, $\sigma = 0.44(0.24)$ for $f = 1/2(1/3)$

IV. DUALITY TRANSFORMATION

In this section, we apply a duality transformation for the qXYM to understand the behavior of vortex observed in the previous section by the eQMC. This approach is an extension of the famous analysis on the 2D classical XY model, see for example Ref.[27, 28]. Duality-transformed model of the qXYM is described in term of the vortex density and topological current field. Besides the vortex-solid formation, it explains the vortex-line fluctuations in the τ -direction controlled by the on-site repulsion U . Furthermore from the dual model, we find the $f = 1/q$ rule for vortex solid pattern, which explains how the vortex-solid pattern is determined by the magnetic field f , the lattice size L , and vortex density-density interaction.

A. Derivation of the dual-qXYM

To derive the dual-qXYM, let us focus on the first and second terms in Eq. (7), and define

$$Z_{\tau+h\text{op}} = \int [d\theta(r)] e^{-S_{\tau+h\text{op}}}, \quad (13)$$

$$S_{\tau+h\text{op}} = - \sum_{r,\tau} \frac{1}{4U} \cos(\theta(r+\tau) - \theta(r)) - \sum_{r,\mu} J \cos(\theta(r+\mu) - \theta(r) + A_\mu(r)), \quad (14)$$

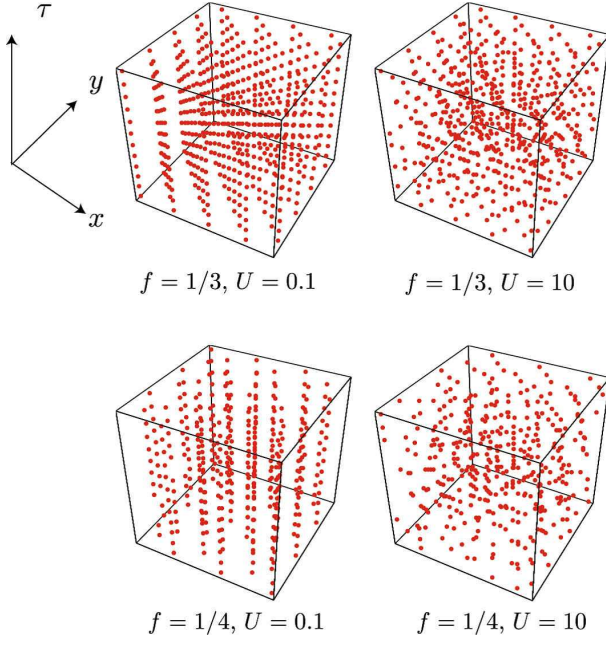


FIG. 5. (Color online) The typical vortex lines in $f = 1/3$ and $1/4$ along the imaginary time direction τ . The red dots are the vortices residing in the dual site r . As the on-site repulsive interaction U increases, the vortex-lines are entangled, and the quantum tunneling from the vortex lattice shown in Fig.3 to another parallel-translated one takes place. When U is small, the vortex solid states does not change along imaginary time direction.

where we have set $\Delta\tau \equiv 1$, $\rho_r = \langle \rho_r \rangle = 1$ for simplicity. (Effects of fluctuations in the local density ρ_r will be discussed in Sec.IV.C and Sec.IV.D.) In the following, we express the action $S_{\tau+hop}$ as follows for notational simplicity,

$$S_{\tau+hop} = - \sum_{r,\mu} J_\mu \cos(\theta(r+\mu) - \theta(r) + A_\mu(r)), \quad (15)$$

where we have redefined direction labels, the couplings, and vector potentials as

$$\mu = 0, 1(\hat{x}), 2(\hat{y}), J_0 = \frac{1}{8U}, J_1 = J_2 = J \quad (16)$$

and use the gauge

$$A_0(r) = 0, A_1(r) = 2\pi f y, A_2(r) = 0. \quad (17)$$

Let us apply the periodic Gaussian approximation to Eq.(13)[27, 28],

$$\begin{aligned} & e^{J_\mu \cos(\theta(r+\mu) - \theta(r) + A_\mu(r))} \\ & \rightarrow \sum_{n_\mu=-\infty}^{\infty} e^{J_\mu} \exp \left[-\frac{J_\mu}{2} \left(\theta(r+\mu) - \theta(r) \right. \right. \\ & \quad \left. \left. + A_\mu(r) - 2\pi n_\mu(r') \right)^2 \right], \end{aligned} \quad (18)$$

where the vector field $n_\mu(r')$ is defined on the sites r' of the 3D dual lattice, and this field represents 2π periodicity of the cosine term in $S_{\tau+hop}$. Substituting Eq. (18) into the partition function Eq.(13), we obtain the following equation by using Poisson formula (see for example, Ref.[27]),

$$\begin{aligned} Z_{\tau+hop} & \propto \int [d\theta(r)] \sum_{l_\mu(r')} \exp \left[- \sum_{r,\mu} \left(\frac{l_\mu^2(r')}{2J_\mu} - i l_\mu(r') (\theta(r+\mu) - \theta(r) + A_\mu(r)) \right) \right] \\ & \propto \sum_{l_\mu(r')} \exp \left(- \sum_{r,\mu} \frac{l_\mu^2(r')}{2J_\mu} - i l_\mu(r) A_\mu(r) \right) \Pi_r \delta \left(\sum_\mu l_\mu(r') - l_\mu(r' - \mu) \right), \end{aligned} \quad (19)$$

where we have used the Hubbard-Stratonovich transformation, and the vector integer field $l_\mu(r')$ has been introduced as the boson-current variables. To solve the δ -function constraint in Eq.(19), we introduce new integer-

gauge fields $\tilde{a}_\mu(r)$, with which $l_\mu(r')$ is expressed as $l_\mu(r') \equiv \frac{1}{2\pi} \epsilon_{\mu\nu\lambda} \nabla_\nu \tilde{a}_\lambda(r')$. By substituting the above expression of $l_\mu(r')$ into the action, we have

$$Z_{\tau+hop} \propto \sum_{\tilde{a}_\mu(r)} \exp \left(- \sum_{r,\mu} \frac{(\epsilon_{\mu\nu\lambda} \nabla_\nu \tilde{a}_\lambda(r))^2}{4\pi J_\mu} - i \epsilon_{\mu\nu\lambda} \nabla_\nu \tilde{a}_\lambda(r) A_\mu(r) \right), \quad (20)$$

where the operator ∇_μ is lattice nabla, defined by

$\nabla_\mu A_\nu(r) \equiv A_\nu(r+\mu) - A_\nu(r)$. Here we use again Poisson

summation formula, and then the integer variables $\tilde{a}_\mu(r')$

are transformed into the continuum variables $\phi_\mu(r')$, and the partition function is expressed as,

$$\begin{aligned} Z_{\tau+hop} &\propto \int_{-\infty}^{\infty} [d\phi_\mu(r')] \sum_{m_\mu(r')} \exp \left(- \sum_{r,\mu} \frac{(\epsilon_{\mu\nu\lambda} \nabla_\nu \phi_\lambda(r'))^2}{4\pi J_\mu} - i\epsilon_{\mu\nu\lambda} \nabla_\nu \phi_\lambda(r') A_\mu(r) + 2\pi i m_\mu(r') \phi_\mu(r') \right) \\ &= \int_{-\infty}^{\infty} [d\phi_\mu(r')] \sum_{m_\mu(r')} \exp \left(- \sum_{r,\mu} \frac{(\epsilon_{\mu\nu\lambda} \nabla_\nu \phi_\lambda(r'))^2}{4\pi J_\mu} - 2\pi i f_\mu \phi_\mu(r') + 2\pi i m_\mu(r') \phi_\mu(r') \right) \\ &\equiv \sum_{m_\mu(r')} \int_{-\infty}^{\infty} [d\phi_\mu(r')] e^{-S_v}, \end{aligned} \quad (21)$$

with

$$S_v(\tilde{j}_\mu(r'), \phi_\mu(r')) = \sum_{r',\mu} \left[-\frac{1}{4\pi J_\mu} (\epsilon_{\mu\nu\lambda} \nabla_\nu \phi_\lambda(r'))^2 + i\phi_\mu(r') \tilde{j}_\mu(r') \right], \quad (22)$$

where we have introduced the three-component flux field $f_\mu(r)$ for the notational simplicity $2\pi f_0(r) = \epsilon_{0ij} \nabla_i A_j(r)$, $f_{1(2)}(r) = 0$, and $\tilde{j}_\mu(r') = 2\pi(m_\mu(r') - f_\mu(r'))$. By integrating the “gauge fields” $\phi_\mu(r')$, we obtain the final expression of the dual model.

As the action S_v in Eq.(22) is invariant under a local gauge transformation $\phi_\lambda(r') \rightarrow \phi_\lambda(r') - \nabla_\lambda \alpha(r')$ with an arbitrary scalar function $\alpha(r')$, we have to fix the gauge of $\phi(r')$ to integrate out $\phi(r')$. To this end, we consider the case of $J_\mu = J$ for simplicity and employ the Lorentz gauge $\sum_{\mu=0,1,2} \nabla_\mu \phi_\mu = 0$. In the present path-integral formalism, this gauge condition is easily imposed by adding the gauge-fixing term $(\sum_\mu \nabla_\mu \phi_\mu)^2$ to the action S_v . In the Lorentz gauge,

$$\begin{aligned} S_v &- \frac{1}{4\pi J} (\sum_{r',\mu} \nabla_\mu \phi_\mu)^2 + (\tilde{j} - \text{terms}) \\ &= \frac{1}{4\pi J} \sum_{r',\mu,\lambda} \phi_\lambda \nabla_\mu^2 \phi_\lambda + (\tilde{j} - \text{terms}). \end{aligned} \quad (23)$$

Integration over $\phi(r)$ in Eq.(21) can be performed straightforwardly and obtain the dual model of the vortex density and vortex current $\tilde{j}_\mu(r')$ as follows,

$$\begin{aligned} \sum_{m_\mu(r')} \int_{-\infty}^{\infty} [d\phi_\mu(r')] e^{-S_v} &= \sum_{m_\mu(r')} e^{-S_{\text{dual}}}, \\ S_{\text{dual}} &= -\frac{\pi}{J} \sum_{r',r''} \tilde{j}_\mu(r') (\sum_\mu \nabla_\mu^2)^{-1}(r, r') \tilde{j}_\mu(r''). \end{aligned} \quad (24)$$

In what follows, we shall study the stationary state of the vortex configurations like the vortex solid. We first interested in the vortex density-density interaction in the dual model, i.e., the interaction between the component \tilde{j}_0 in Eq.(24), and evaluate the corresponding term as

$$-\pi J \sum_{r'} \tilde{j}_0(r) \frac{1}{\nabla_1^2 + \nabla_2^2} \tilde{j}_0(r') = \pi J \sum_{\text{B.Z.}} \tilde{j}_0(k) \frac{1}{|k|^2} \tilde{j}_0(-k), \quad (25)$$

where $\tilde{j}_\mu(r) = \sum_{\text{B.Z.}} \tilde{j}_\mu(k) e^{ikr}$ (B.Z. refers to the first Brillouin Zone) and $\tilde{k}_\mu = \frac{2}{a_L} \sin \frac{k_\mu a_L}{2}$. The same result with Eq.(25) is obtained in the Coulomb gauge $\sum_{\alpha=1,2} \nabla_\alpha \phi_\alpha = 0$. In the long-distance region $|r' - r''| \gg a_L$, Eq.(25) behaves as

$$\begin{aligned} &\pi J \sum_{\text{B.Z.}} \tilde{j}_0(k) \frac{1}{|k|^2} \tilde{j}_0(-k) \\ &\sim \pi J \sum_{r',r''} \tilde{j}_0(r') \sum_k \frac{1}{k^2} e^{-ik(r' - r'')} \tilde{j}_0(r'') \\ &\propto \pi J \sum_{r',r''} \tilde{j}_0(r') \log |r' - r''| \tilde{j}_0(r'') + \alpha \left(\sum_{r'} \tilde{j}_0(r') \right)^2 \\ &= \pi J \sum_{r',r''} (j_0(r') - 2\pi f) \log |r' - r''| (j_0(r') - 2\pi f) \\ &\quad + \alpha \left(\sum_{r'} (j_0(r') - 2\pi f) \right)^2. \end{aligned} \quad (26)$$

where $j_\mu(r') \equiv 2\pi m_\mu(r')$, and we have introduced the α -term by regularizing the infrared divergence in the k -integration and then $\alpha \sim \ln(L/a_L)$. It is easily verified that the current-current correlations $(j_1 - j_1)$ and $(j_2 - j_2)$ -terms have a similar form with Eq.(26), but its coefficient is $1/4U$. Therefore as U is getting large, the current correlation becomes weak and nontrivial configurations of the current $\vec{j} = (j_1, j_2)$ appear. This means the correlation of vortex density in the τ -direction is getting weak as we observed in the numerical simulations in Fig.5. In following section, we explain the generated patterns of the vortex solid by the eQMC from Eq.(26).

B. Vortex solid $f = 1/q$ rule

In previous section, we derived the dual-qXYM model. For the stationary configurations, the vortex-density in-

interaction has the logarithmic form similar to that of 2D XY model, and its coefficient is proportional to the hopping amplitude J . Moreover, the infrared singularity gives the “charge-neutrality condition” as

$$\left(\sum_{r'} \tilde{j}_0(r')\right)^2 \propto \left(\sum_r (2\pi m_0(r) - 2\pi f)\right)^2 \rightarrow 0. \quad (27)$$

Thus for sufficiently large hopping J , the BEC is realized in the system and the above condition decides the total number of vortex in the system (more precisely, the number of (vortex – anti-vortex)). Here, we again show the vortex-density interactions,

$$J \sum_{r,r'} (2\pi m_0(r) - 2\pi f) \log |r - r'| (2\pi m_0(r') - 2\pi f) + \alpha \left(\sum_r (2\pi m_0(r) - 2\pi f)\right)^2. \quad (28)$$

From the above interactions, we qualitatively explain the patterns of vortex-solid observed by eQMC in the previous section. For simplicity, we shall consider the case of the magnetic flux $f = 1/q$.

1. In the neutrality condition Eq.(27), $f = 1/q$ and $m_0(r)/2\pi$ is an integer. q adjacent plaquettes have to be grouped for making $q \times 1/q = 1$ flux quantum. To achieve this globally, the lattice system size has to be $qN_x \times qN_y$ (N_x and N_y are natural numbers). This is the lattice size condition of the system.
2. The lattice system is divided into a number of q -adjacent plaquettes. One quantized vortex resides in arbitrary one of q -adjacent plaquettes. To realize low-energy configurations, the vortex density interactions have to be minimized. This decides the distribution pattern of a number of vortices.
3. The number of the distribution pattern corresponds to the number of the degenerate state of the $f = 1/q$ vortex-solid state. When the particle density is high enough, a superposed vortex-solid patterns is realized because of the long-range repulsion between vortices.

The above consideration can be easily extended to the more general cases with $f = p/q$ (p and q are co-prime), and from this consideration it is expected that all possible vortex solids can be observed by the present eQMC simulations

C. Phase diagram in dilute boson regime

In Fig.6, we show the phase diagram of vortex state in the low density regime. As explained in Ref.[29], recent experiments can decrease the atomic density without losing the phase coherence by applying a micro-wave to local regimes of the OL and blowing away excited atoms from the OL. By eQMC calculation, we found that as the average density of bosons is decreased, the vortex-solid states

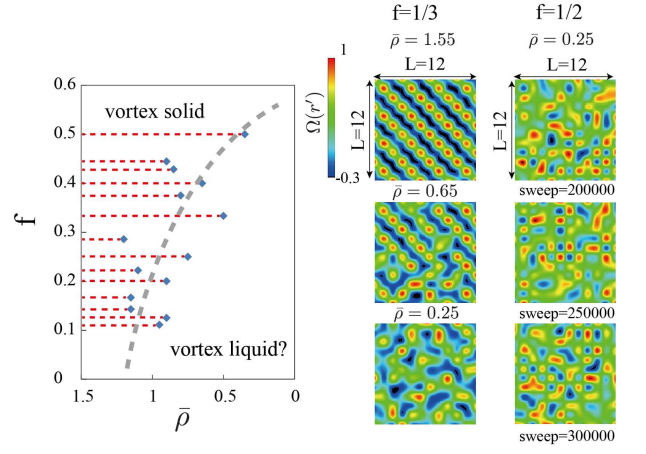


FIG. 6. Numerical results of the dilute density regime. (Left panel) The phase diagram in the $\bar{\rho} - f$ plane. The red broken lines show the observed vortex solid states in which the vortices are pinned on the dual lattice. (Right panel) Snapshots for $f = 1/3$. At $\bar{\rho} = 2$, the robust vortex solid forms. As the density is decreased, ‘melting’ of solid takes place. At present, we do not have clear understanding of the states in the dilute regime. However, we expect that they are a kind of vortex-liquid state. In the right column, we show the results for $f = 1/2$ and $\bar{\rho} = 0.25$, in which a bosonic fractional Hall state is expected to form. The state is rather homogeneous but slightly unstable against the MC updates.

disappear. As shown in Fig.6, locations of vortices do not exhibit any spatial patterns in the low-density region and the transition may be interpreted as a melt of the vortex solid to a vortex liquid[7]. Specific heat C shows a sharp peak at the transition point for some values of f , but for other values of f there is only a moderate peak in C . Due to the diluteness of bosons, the effect of the lattice is weekend and the system approaches to the continuum system. Pining of vortex by the lattice is less effective, and the topological vortex number is spread rather wide spatial regions. These findings are in agreement with the intuitive picture such that for the low-density limit, the lattice works simply as a mesh employed for numerical study. In fact, the low-density limit means small hopping parameter $J(\rho_r \rho_{r+\mu})^{1/2}$ and its relatively large local fluctuations, and then the interaction term in Eq.(28) becomes less effective. This observation is quite instructive for the discussion on the realization of the bosonic Laughlin state in the following section.

D. Bosonic Laughlin state and Chern-Simons theory of the Bose Hubbard Model

In recent years, it was suggested that a state similar to the bosonic Laughlin state forms in the Bose gas system loaded on the OL. In the first-quantization language and also in the continuum space, the bosonic Laughlin state

is given by the following wave function[30],

$$\Psi(z_1, z_2, \dots, z_N) = \prod_{j < k} (z_j - z_k)^m e^{-\frac{1}{4} \sum |z_j|^2}, \quad (29)$$

where $z_j = x_j + iy_j$ and m is an even positive integer. From Eq.(29), it is obvious that bosons in the Laughlin state have the hard-core nature as $\Psi \rightarrow 0$ for $z_j \rightarrow z_k$ ($j \neq k$). In the previous work[8, 9], a numerical diagonalization of a small system showed that the ground-state of the hard-core BHM has a good overlap with the wave function in Eq.(29) for a weak magnetic field $f < 0.2$ and low density $\bar{\rho} < 0.1$ case.

It is interesting to ask if a state that has similar properties to the Laughlin state forms in the boson gas system on the OL for relatively large f 's and particle density. Such a state has a certain hidden order and low-energy excitations behave like anyons. To study this problem, Chern-Simons (CS) theory for the fractional quantum Hall effect (FQHE) is quite useful. We previously introduced a lattice version of the CS theory that is well suited for studying the present system[31].

By using this formalism, we transform the original boson operator a_r in Eq.(1) to another boson operator b_r , which we call CS boson, by attaching m -magnetic flux to a_r ,

$$a_r = V_r b_r, \\ V_r = \exp \left[im \sum_{x'} \theta(r, x') (a_{r'}^\dagger a_{r'}) \right], \quad (30)$$

where x (x') denotes a site of the dual lattice paired to site r (r') of the original lattice, and $\theta(r, x')$ is the azimuthal angle function on the lattice. Please notice $a_r^\dagger a_r = b_r^\dagger b_r$. Then, let us consider the specific case $f = m\bar{\rho}$ where $\bar{\rho}$ is again the average particle density. In this case in terms of the CS boson b_r , the BHM Hamiltonian in Eq.(1) is expressed as,

$$H_{\text{BH}} = -J \sum_{r, \mu} b_r^\dagger W_r^\dagger W_{r+\mu} b_{r+\mu} + \text{h.c.} \\ + \sum_r U (b_r^\dagger b_r)^2, \quad (31)$$

$$W_r = \exp \left[im \sum_{x'} \theta(r, x') (b_{r'}^\dagger b_{r'} - \bar{\rho}) \right], \quad (32)$$

where we have employed the symmetric gauge for $A_\mu(r)$, and used the identity $2\pi\epsilon_{\mu\nu}\nabla_\nu G(x, x') = \nabla_\mu \theta(r, x')$ [$\epsilon_{12} = -\epsilon_{21} = 1, \epsilon_{11} = \epsilon_{22} = 0$] with the two-dimensional lattice Green function $G(x, x')$. Beautiful CS gauge theory can be constructed for the system Eqs.(31) and (32) in the Lagrangian formalism, but here we only discuss the possible mean-field (MF) solution to the ground-state of the above system.

The MF analysis indicates the naive candidate for the ground-state of H_{BH} in Eq.(31) such as $b_r^{\text{MF}} = \bar{\rho}^{1/2}$, i.e., in which the BEC of the CS boson b_r takes place. From Eq.(30) and $f = m\bar{\rho}$, this MF solution accompanies the homogeneous ‘condensation’ of the $2\pi f$ flux quanta per

plaquette to cancel out the external magnetic field. This MF state corresponds to the bosonic Laughlin state and therefore in the bosonic Laughlin state, the grand-state has the homogeneous particle density $\bar{\rho}$ and also the homogeneous vortex density $2\pi f$ per site and per plaquette, respectively. However for sufficiently large $\bar{\rho}$ and f , the above condition is not satisfied by the configuration of a_r because the duality transformation shows that vortex density at each plaquette $m_0(r')$ takes an integer value. This is nothing but the lattice pinning effect of the vortex.

On the other hand for small $\bar{\rho}$ and f , the fluctuations of the parameter $J(\rho_r \rho_{r+\mu})^{1/2}$ cannot be neglected and therefore the direct application of the result of the duality-transformation is questioned. It is quite useful to study, for example, the case with $f = 0.5$, $\bar{\rho} = 0.25$ and therefore $m = 2$. Snapshot of the topological number (vortex density) is shown in Fig.6. It is obvious that a genuine homogeneous configuration is not realized there but topological number tends to smear compared with the higher-density case in Figs.3 and 6. This result seems to indicate the possibility of the bosonic Laughlin state for very low particle density as indicated by the work on the very small systems in Ref[8, 9]. Methods in the present paper are also applicable for the study of such low density cases, i.e., the hard-core BH model. To this end, the slave-particle representation for the hard-core boson is quite useful[32]. This problem is under study and we hope that the results will be reported in another publication in future.

V. HALDANE BOSE-HUBBARD MODEL STUDIED BY eQMC

Recent experiments on cold atoms succeeded in realizing the Haldane-Bose-Hubbard model in a honeycomb optical lattice[33]. This system is a bosonic analog of the celebrated Haldane model[20], which is a fermionic system and possesses a topological phase due complex hopping amplitudes on the honeycomb lattice. Besides the NN and NNN hopping terms, the on-site repulsion exists in the HBHM, and as result of the competition of these three terms, the model has a rich phase diagram. The HBHM realized by cold atomic gases on the optical lattice is highly controllable, e.g., besides the average particle density, the on-site repulsion, the hopping amplitude and the artificial magnetic flux generated by the NN hopping can be controlled.

In this section, we shall study the HBHM by means of the eQMC and obtain the global phase diagram. To this end, we calculate the internal energy, specific heat and certain correlation functions to identify order of phase transitions and physical properties of phases. By using the FSS, we obtain the critical exponents for phase transitions. The previous work[21] clarified the phase diagram of the HBHM, however the system size in the numerical calculation (the exact diagonalization) is small, and only the case of unit filling was considered. Therefore

the present study using the eQMC is complementary to the previous work. In particular, besides those found in Ref.[21] we have found another phase boundary.

As in Ref.[21], the Hamiltonian of the HBHM is given by

$$H_{\text{HBH}} = -J_1 \sum_{\langle i,j \rangle} a_i^\dagger a_j - J_2 \sum_{\langle\langle i,j \rangle\rangle} e^{-i\phi} a_i^\dagger a_j + U \sum_i a_i^\dagger a_i a_i^\dagger a_i, \quad (33)$$

where $\langle i,j \rangle$ denotes NN sites, $\langle\langle i,j \rangle\rangle$ NNN sites of the honeycomb lattice. The parameters J_1 and J_2 are the NN and NNN hopping amplitudes, respectively, and ϕ is a constant phase of the NNN hopping. By a calculation similar to that in Sec.II, the effective action for the HBHM is obtained as

$$S_{\text{HBH}} = \int d\tau \left(- \sum_i \frac{1}{4U} (i\partial_\tau \theta(i))^2 - J_1 \sum_{\langle i,j \rangle} \sqrt{\rho_i \rho_j} \cos(\theta_i - \theta_j) - J_2 \sum_{\langle\langle i,j \rangle\rangle} \sqrt{\rho_i \rho_j} \cos(\theta_i - \theta_j + \phi) \right). \quad (34)$$

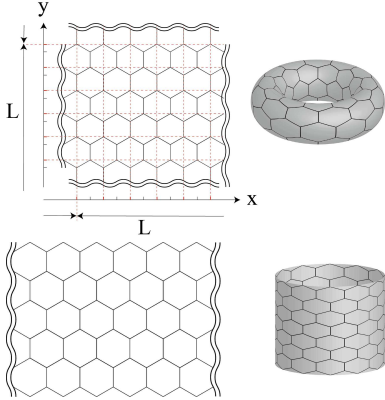


FIG. 7. (Color online) Honeycomb lattice with the periodic boundary condition (torus) and also that of the cylinder geometry. The system size can be defined from A sub-lattice size, its lattice is a square $L \times L$ lattice. The imaginary-time τ lattice is fixed $L_\tau = 8$ and has periodic boundary condition.

For the numerical calculation, we consider the following system;

1. We consider the unit-filling case and in most of the calculations we set the variational parameters $\rho_i = \rho = 1$ for simplicity. Full MC simulation of the action (34) verifies the validity of the above assumption.
2. We put $\phi = \pi/2$ as in Ref.[21].
3. Both the torus and cylinder geometries are considered. See Fig.7.

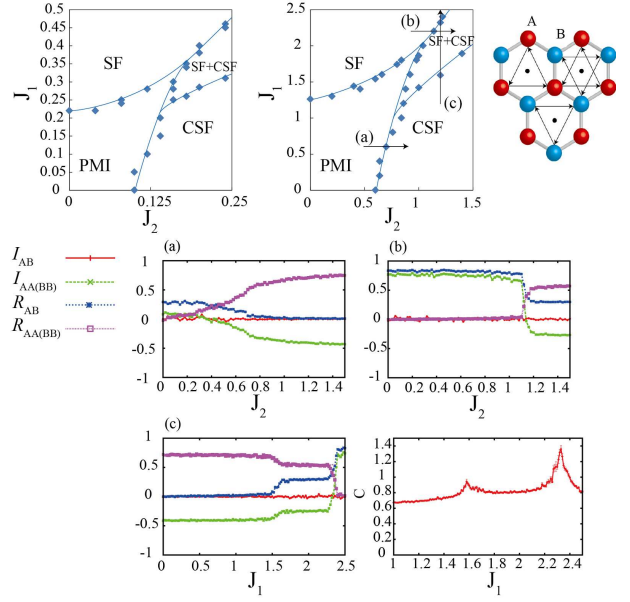


FIG. 8. Phase diagrams of HBHM with $U = 0.1$ (top left) and $U = 10$ (top middle). Calculations of the various physical quantities are shown, which are used for identification of the phases. Between the SF and CSF, there exists a coexisting SF+CSF phase. “Specific heat” C along the line (c) in the phase diagram (bottom right) exhibits two peaks at $J_1 \simeq 1.6$ and 2.3 . The system size is $L = 6$

4. To classify the physical meaning of the observed states, we measure the current operators defined as

$$I_{ij} \equiv 2 \operatorname{Im} \left(J_{ij} \langle e^{i(\theta_i - \theta_j)} \rangle \right), \quad (35)$$

and also the link correlation defined by,

$$R_{ij} \equiv 2 \operatorname{Re} \left(J_{ij} \langle e^{i(\theta_i - \theta_j)} \rangle \right), \quad (36)$$

where J_{ij} is J_1 and $J_2 e^{i\phi}$ for the links connecting NN and NNN sites, respectively.

As explained in the previous work Ref[21], for small J_1/U and J_2/U , the system is the plaquette Mott insulator (PMI) that has only finite local correlation $I_{AA(BB)}^{\text{PMI}} \neq 0$ and vanishing nonlocal correlations. On the other hand for a large $J_1 \gg J_2$, the ordinary superfluid (SF) forms and it has a positive expectation value $I_{AA(BB)}^{\text{SF}} > 0$ and $I_{AB}^{\text{SF}} = 0$. For the weakly interacting limit, $I_{AA(BB)}^{\text{SF}} = 2\rho J_2$. For $J_1 \ll J_2$, the J_2 -term in the Hamiltonian Eq.(33) dominates and the chiral SF (CSF) forms with a negative expectation value $I_{AA(BB)}^{\text{CSF}} < 0$. For the weakly interacting limit, $I_{AA(BB)}^{\text{CSF}} = -2\rho J_2$.

In this work, the HBHM is studied by the eQMC and the phase boundaries are identified by calculating the internal energy E and the “specific heat” C as in the study on the BH model in the previous section. We furthermore calculate the density of states, $N(S)$, to identify the order

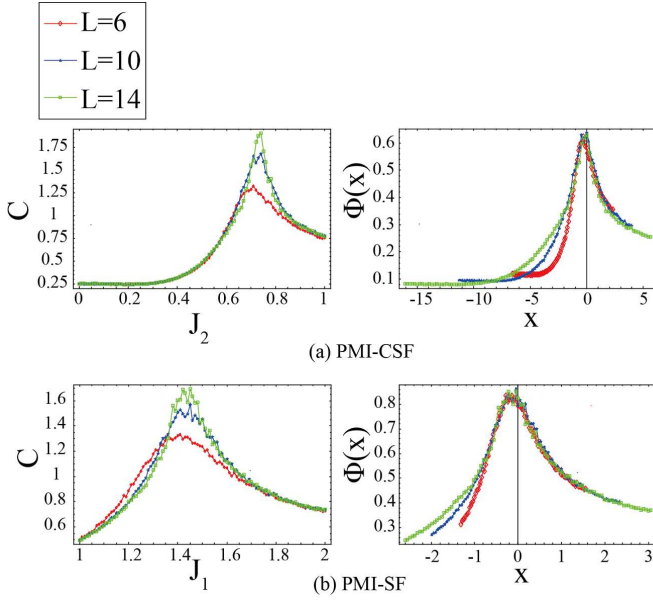


FIG. 9. “Specific heat” C and the scaling function of the FSS $\Phi(x)$. Upper panels, the PMI-CSF phase transition. Lower panels, the PMI-SF phase transition. FSS indicates that both phase transitions are of second order. $U = 10$.

of phase transitions, which is defined as

$$\begin{aligned}
 Z_{\text{HBH}} &= \int [d\theta(r)] e^{-S_{\text{HBH}}} \\
 &= \int dS e^{-S} \int [d\theta(r)] \delta(S - S_{\text{HBH}}) \\
 &= \int dS e^{-S} N(S).
 \end{aligned} \quad (37)$$

On a phase transition point, we calculate $N(S)$ by the MC simulations. If $e^{-S}N(S)$ has a double-peak shape as a function of S , the phase transition is of first order, whereas a single-peak shape of $e^{-S}N(S)$ indicates a second-order transition.

We first consider the system with the periodic boundary condition, i.e., a torus. Fig.8 exhibits the global phase diagrams of the HBHM with $U = 0.1$ and 10 . In the phase diagram, there are four phases, three of which are found in the previous work[21], i.e., the PMI, SF, and CSF. The fourth phase is a coexisting phase possessing both the SF and CSF correlations. Calculated “specific heat” C is shown in Fig.8 as a function of J_1 , which indicates the existence of two phase transitions for $J_2 = 1.2$ and $U = 10$. The NN and NNN currents are calculated for the identification of the phase and the results are shown in Fig.8. In the SF, the intra-sublattice current $I_{AA}^{\text{SF}} > 0$, whereas in the CSF $I_{AA}^{\text{CSF}} < 0$ as explained in Ref.[21]. In the SF+CSF coexisting phase, the value of I_{AA} , I_{AA}^{co} , is $I_{AA}^{\text{CSF}} < I_{AA}^{\text{co}} < I_{AA}^{\text{SF}}$. Phase diagram of other values of U has qualitatively the same structure with that in Fig.8. However, as decreasing on-site interaction U , the phase boundary shifts because of the suppression of quantum fluctuations of the phase θ_i , which

are induced by growing density fluctuations. “Specific heat” C and the scaling function of the FSS are shown in Fig.9. The results indicate that both the PMI-SF and PMI-CSF transitions are of second order. The critical exponents are estimated as $\nu = 0.95(1.25)$, $\sigma = 0.42(0.26)$ for PMI-SF (PMI-CSF). On the other hand for the phase transition from the SF to the SF+CSF phase and also from the CSF to the SF+CSF phase, the calculated C for various system sizes does not exhibit the FSS, nor the density of states $N(S)$ defined by Eq.(37) exhibits a double-peak shape at the phase transition point. More detailed study using a large-scale systems is needed to clarify the properties of the phase transition SF (CSF) \rightarrow SF+CSF.

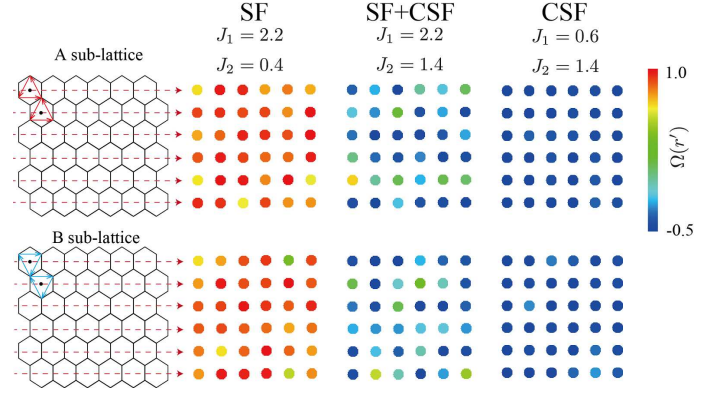


FIG. 10. Snapshots of vortex Ω_A and Ω_B in the SF, CSF and SF+CSF phases. In the SF, phase of BEC has a uniform distribution. On the other hand in the CSF, 120° -structure forms. In the SF+CSF phase, a spatial mixture of them appears.

It is interesting to see if a vortex solid forms in the SF and CSF phases, and in particular how the vortex solid is deformed by the coexistence of the SF and CSF in the SF+CSF phase. To this end, we calculate the triangle vorticity of the A and B -sublattices, $\Omega_{A(B)}(r)$, which is defined by

$$\begin{aligned}
 \Omega_{A(B)}(r) &= \frac{1}{3} \left(\sin(\theta_2 - \theta_1 + \phi) + \sin(\theta_3 - \theta_2 + \phi) \right. \\
 &\quad \left. + \sin(\theta_1 - \theta_3 + \phi) \right),
 \end{aligned} \quad (38)$$

where the detailed definition of θ 's, see Fig.10 and $\phi = \pi/2$ in the present case. For the configuration of the uniform $\theta_i(r)$, $\Omega_{A(B)}(r) = 1$, whereas for the 120° -configuration, $\Omega_{A(B)}(r) = -1/2$. Snapshots of $\Omega_{A(B)}(r)$ are shown in Fig.10, and the results indicate that the uniform- θ configurations are realized in the SF, whereas nearly 120° -configurations are in the CSF, as expected. On the other hand, the SF+CSF phase has a nontrivial distribution of the vortex. From this result, we expect that immiscible SF droplets exist in the CSF and vice versa in the SF+CSF state.

Finally, let us study the HBHM in the cylinder geometry shown in Fig.7. In particular we are interested in

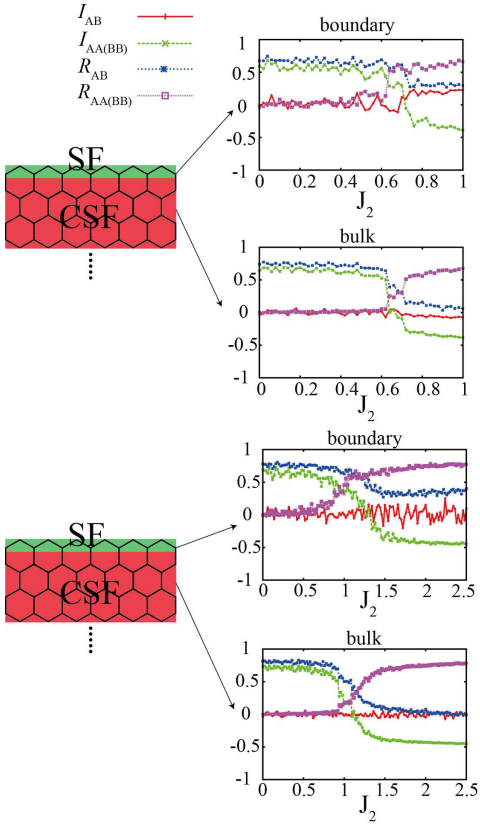


FIG. 11. Phase diagrams of HBHM in the cylinder geometry. Calculations of the various physical quantities are shown, which are used for identification of the phases. Near zigzag edges, the quasi-one-dimensional SF state forms in the bulk CSF state. Upper panel for $U = 0.5$ and lower panel $U = 1.0$. The system size is $L = 6$

BEC behavior near the zigzag edges of the cylinder. In recent experiments, such a sharp edge boundary can be created by using the optical-box trap method[34]. For the SF phase of the HBHM, Bogoliubov excitations near the edges was recently studied[35]. On the other hand in the present study, we focus on the SF+CSF phase that was observed by the eQMC in the previous section. It is expected that near the edges a quasi-one-dimensional excitation forms and the J_1 -term in Eq.(33) dominates there. Therefore, the SF state appears near the edges of the cylinder. This expectation is verified by calculating I_{ij} and R_{ij} . See Fig.11. Schematic picture is that for the bulk CSF state, the SF state appears near the edge of the

cylinder BEC, whose bulk state is the CSF for $J_2 > J_{2c}$, where J_{2c} is the critical value of J_2 . On the other hand for smaller $J_2 < J_{2c}$, the whole system is the SF.

VI. CONCLUSION

In this paper, we studied the BHM and HBHM with complex hopping amplitudes that are recently realized by experiments of the cold atoms[2, 3, 33]. We first explained the numerical methods that we call the eQMC. Most of the numerical results in the present paper have been obtained by the eQMC.

For the BHM in various magnetic fields, we focused on the vortex-solid state and clarified its existence for various flux quanta $f = p/q$. Various spatial patterns of the vortex-solid have been identified by calculating the winding number for each lattice plaquette. We furthermore found that the on-site repulsion U plays an important role for the phase transition from the vortex solid to vortex liquid. By the duality transformation of the effective mode of the BHM, we discussed the condition on f for the formation of the vortex solid.

For the HBHM, we have obtained the global phase diagram of the ground-state with the complex NNN hopping with $\phi = \pi/2$. Besides those found in Ref.[21], we have found another phase in which the SF and CSF regions co-exist. Uniform and 120° structures of the phase degrees of the freedom of the condensed boson field are ‘entangled’ with each other. More detailed study is needed to clarify the dynamical properties of the SF+CSF phase like a quantum (in)stability, etc. This is a future problem. Finally, we studied the SF+CSF state of the HBHM in the cylinder geometry, and found that the quasi-1D SF state appears near the edges of the cylinder. This phenomenon might have some connection to the edge state in the quantum Hall like state. This is also a future problem.

ACKNOWLEDGMENTS

Y. K. acknowledges the support of a Grant-in-Aid for JSPS Fellows (No. 15J07370). This work was partially supported by Grant-in-Aid for Scientific Research from Japan Society for the Promotion of Science under Grant No.26400246.

[1] I. Bloch, J. Dalibard, and W. Zwerger, Rev. Mod. Phys.**80**, 885 (2008); M. Lewenstein, A. Sanpera, and V. Ahufinger, *Ultracold Atoms in Optical Lattices: Simulating Quantum Many-body Systems* (Oxford University Press, 2012).

[2] M.Aidelsburger, M.Atala, S.Nascimbene, S.Trotzky, Y.-A.Chen, and I.Bloch, Phys. Rev. Lett. **107**, 255301 (2011);

[3] M. Aidelsburger, M. Atala, M. Lohse, J. T. Barreiro, B. Paredes, and I. Bloch, Phys. Rev. Lett. **111**, 185301 (2013); H. Miyake, G. a. Siviloglou, C. J. Kennedy, W. C.

- Burton, and W. Ketterle, Phys. Rev. Lett. **111**, 185302 (2013).
- [4] D. Jaksch and P. Zoller, New J. Phys. **5**, 56, (2003).
- [5] S. Tung, V. Schweikhard, and E. A. Cornell, Phys. Rev. Lett. **97**, 240402 (2006); R. A. Williams, S. Al-Assam, and C. J. Foot, Phys. Rev. Lett. **104**, 050404 (2010).
- [6] S. Furukawa and M. Ueda, Phys. Rev. Lett. **111**, 090401 (2013).
- [7] N. Cooper, N. Wilkin and J. Gunn, Phys. Rev. Lett. **87**, 120405 (2001).
- [8] A. Sørensen, E. Demler and M. Lukin, Phys. Rev. Lett. **94**, 086803 (2005).
- [9] M. Hafezi, A. Sørensen, E. Demler and M. Lukin, Phys. Rev. A **76**, 023613 (2007).
- [10] G. Moller and N. Cooper, Phys. Rev. Lett. **103**, 105303 (2009); L. Hormozi, G. Moller and S. H. Simon, Phys. Rev. Lett. **108**, 256809 (2012); R. O. Umucalilar and M. O. Oktel, Phys. Rev. A **76**, 055601 (2007).
- [11] R. Bhat, M. Holland and L. Carr, Phys. Rev. Lett. **96**, 060405 (2006); R. Bhat, M. Kramer, J. Cooper and M. Holland, Phys. Rev. A **76**, 043601 (2007); R. Bhat, B. Peden, B. Seaman, M. Kramer, L. Carr and M. Holland, Phys. Rev. A **74**, 063606 (2007).
- [12] E. Lundh, Europhys. Lett. **84**, 10007 (2009).
- [13] M. Y. Choi and S. Doniach, Phys. Rev. B **31**, 4516 (1985).
- [14] Y. Nakano, K. Kasamatsu, and T. Matsui, Phys. Rev. A **85**, 023622 (2012).
- [15] K. Kasamatsu, Phys. Rev. A **79**, 021604(R) (2009).
- [16] T. Duri and D. K. K. Lee, Phys. Rev. B **81**, 014520 (2010).
- [17] A. Kato, Y. Nakano, K. Kasamatsu, and T. Matsui, Phys. Rev. A **84**, 053623 (2011).
- [18] K. Kasamatsu, J. Low Temp. Phys. **150**, 593 (2007).
- [19] Y. Kuno, K. Suzuki, and I. Ichinose, J. Phys. Soc. Jpn. **82**, 124501 (2013).
- [20] F. D. M. Haldane, Phys. Rev. Lett. **61**, 2015 (1988).
- [21] I. Vasic, A. Petrescu, K. Le Hur, and W. Hofstetter, Phys. Rev. B **91**, 094502 (2015).
- [22] S. D. Huber, B. Theiler, E. Altman, and G. Blatter, Phys. Rev. Lett. **100**, 050404 (2008); S. Gazit, D. Podolsky, and A. Auerbach, Phys. Rev. Lett. **110**, 140401 (2013).
- [23] U. Bissbort, S. Go. Ntze, Y. Li, J. Heinze, J. S. Krauser, M. Weinberg, C. Becker, K. Sengstock, and W. Hofstetter: Phys. Rev. Lett. **106**, 205303 (2011); M. Endres, T. Fukuhara, D. Pekker, M. Cheneau, P. Schau, C. Gross, E. Demler, S. Kuhr, and I. Bloch: Nature **487**, 454 (2012).
- [24] Y. Kuno, K. Suzuki, and I. Ichinose, J. Phys. Soc. Jpn. **83**, 074501 (2014); Y. Kuno, K. Suzuki, and I. Ichinose, Phys. Rev. A **90**, 063620 (2014).
- [25] N. Metropolis, A. W. Rosenbluth, M. N. Rosenbluth, A. M. Teller, and E. Teller, J. Chem. Phys. **21**, 1087 (1953); J. M. Thijssen, Computational Physics (Cambridge University Press, Cambridge, 1999).
- [26] D. R. Hofstadter, Phys. Rev. B **14**, 2239 (1976).
- [27] R. Savit, Rev. Mod. Phys. **52**, 453 (1980); J. B. Kogut, T. Banks, and R. Myerson, Nucl. Phys. B **129**, 493 (1977).
- [28] N. Nagaosa, *Quantum Field Theory in Condensed Matter Physics* (Springer, 1999).
- [29] C. Weitenberg, M. Endres, J. F. Sherson, M. Cheneau, P. Schauss, T. Fukuhara, I. Bloch, and S. Kuhr, Nature **471**, 319 (2011).
- [30] R. B. Laughlin, Phys. Rev. Lett. **50**, 1395 (1983).
- [31] I. Ichinose and T. Matsui, Nucl. Phys. B **468** [FS], 487 (1996); Nucl. Phys. B **483** [FS], 681 (1997).
- [32] See for example, Y. Nakano, T. Ishima, N. Kobayashi, K. Sakakibara, I. Ichinose, and T. Matsui, Phys. Rev. B **83**, 235116 (2011); Y. Nakano, T. Ishima, N. Kobayashi, T. Yamamoto, I. Ichinose, and T. Matsui, Phys. Rev. A **85**, 023617 (2012).
- [33] G. Jotzu, M. Messer, R. Desbuquois, M. Lebrat, T. Uehlinger, D. Greif, and T. Esslinger, Nature **515**, 237 (2014).
- [34] A. L. Gaunt, T. F. Schmidutz, I. Gotlibovych, R. P. Smith, and Z. Hadzibabic, Phys. Rev. Lett. **110**, 200406 (2013).
- [35] S. Furukawa and M. Ueda, arXiv:1506.04556.